



A practical method to simulate realistic reduced-exposure CT images by the addition of computationally generated noise

Nicholas Mark Gibson¹ · Amy Lee² · Martin Bencsik²

Received: 2 May 2023 / Revised: 16 October 2023 / Accepted: 17 October 2023 / Published online: 13 November 2023
© Crown 2023

Abstract

Computed tomography (CT) scanning protocols should be optimized to minimize the radiation dose necessary for imaging. The addition of computationally generated noise to the CT images facilitates dose reduction. The objective of this study was to develop a noise addition method that reproduces the complexity of the noise texture present in clinical images with directionality that varies over images according to the underlying anatomy, requiring only Digital Imaging and Communications in Medicine (DICOM) images as input data and commonly available phantoms for calibration. The developed method is based on the estimation of projection data by forward projection from images, the addition of Poisson noise, and the reconstruction of new images. The method was validated by applying it to images acquired from cylindrical and thoracic phantoms using source images with exposures up to 49 mAs and target images between 39 and 5 mAs. 2D noise spectra were derived for regions of interest in the generated low-dose images and compared with those from the scanner-acquired low-dose images. The root mean square difference between the standard deviations of noise was 4%, except for very low exposures in peripheral regions of the cylindrical phantom. The noise spectra from the corresponding regions of interest exhibited remarkable agreement, indicating that the complex nature of the noise was reproduced. A practical method for adding noise to CT images was presented, and the magnitudes of noise and spectral content were validated. This method may be used to optimize CT imaging.

Keywords X-ray computed tomography · Radiation dose reduction · Low-dose simulation · Noise modelling · Two-dimensional noise spectra

1 Introduction

Computed tomography (CT) has been widely used in medicine over the past four decades because of its high diagnostic value for a broad range of pathologies. However, CT imaging is associated with a relatively high ionizing radiation dose to patients and, consequently, with the risk of late stochastic effects, such as carcinogenesis, over which there is an established concern [1]. Several efforts have been made in the field of CT imaging to optimize the scanning protocols and to identify the lowest dose adequate for scanning the

patients as per the ALARP (as low as reasonably practicable) principle [2–4]. Some studies have utilized repeated scanning of patients or volunteers at different dose settings [5–7]; however, because of the additional doses incurred by the patient/volunteer, this is ethically undesirable. Therefore, there has been great interest in the development of tools based on computational methods to add realistic noise to CT images to simulate lower-exposure images and reduce the radiation dose. This aids in optimizing the imaging technique without requiring repeated patient scanning.

Computed tomography (CT) image noise is complex. Owing to the progress made in scanner design, noise characteristics have been studied in detail, including noise power spectra (NPS) for a simple parallel-beam geometry [8, 9], the effect of interpolation on the filtered back-projection process [10], the effect of helical scanning [11], fan-beam geometry [12, 13], and multidetector CT [14]. Quantum (as opposed to electronic) noise is structured directionally and oriented in the direction of highest attenuation in the field of view

✉ Nicholas Mark Gibson
nick.gibson@nuh.nhs.uk

¹ Medical Physics and Clinical Engineering, Queens Medical Centre, Nottingham University Hospitals NHS Trust, Derby Road, Nottingham NG7 2UH, UK

² Physics and Mathematics, Nottingham Trent University, Clifton Lane, Clifton, Nottingham NG11 8NS, UK

[15]. This is illustrated in the attenuating cylinder shown in Fig. 1. The noise in radiographic images of the shoulder and hip regions is often the most pronounced because of the more highly attenuated X-ray paths encountered in the lateral direction compared with the a.p. direction [15, 16]. Owing to the high level of nonuniformity in the incident flux across the detector data, the noise characteristics vary with the position in the field of view and the imaging subject. This structured, directionally oriented noise can affect lesion detectability [9, 12]. For example, nonuniform noise is often observed through the femoral heads, which hinders the visualization of important structures such as pelvic lymph nodes. Any noise addition tool used to study this phenomenon must fully reproduce this characteristic.

Several methods have been deployed to add noise to CT images computationally. Britten [17] used a method based on generating Gaussian noise and coloring it by convolving it with an autocorrelation function derived from a water phantom image, which was assessed using brain CT images. However, this method cannot reproduce a characteristic with either directionality or variation between different regions of the field of view. Frush [14], Massoumzadeh [18], Joemai [19], Yu [20], Kalendar [15], Zabic [21], and Zeng [22], used methods based on extracting detector profile data from scanners and adding

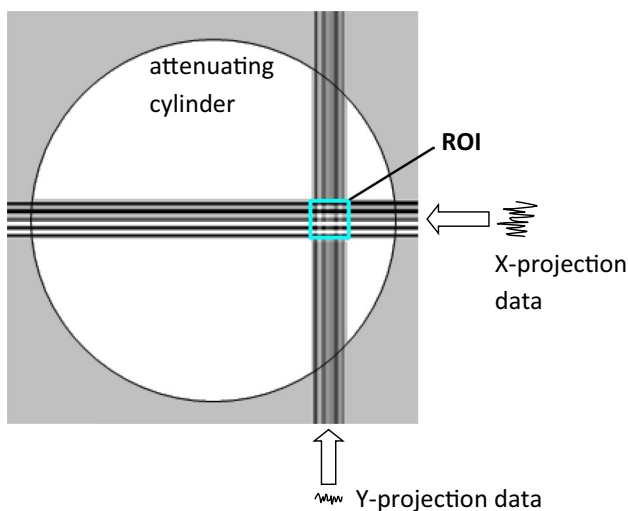


Fig. 1 Illustration of directional noise in an image of an attenuating cylinder. Projections are shown for the reconstruction of the region of interest ROI; the X-projection has passed through more attenuation and, therefore, has a higher level of quantum noise than the Y-projection, which is more peripheral. Hence, noise from the X-projection is more dominant in the ROI, generating an overall noise oriented in the X-direction, that is, along the direction from the center of the cylinder to the ROI, which is the direction of the highest attenuation. As the region moves around the periphery of the cylinder, the orientation of noise remains towards the center of the cylinder. At the very center of the cylinder, attenuation is equal in all directions; therefore, the noise is non-directional

noise to the profile data before reconstructing the images. These methods successfully reproduce complex directional characteristics; however, a major drawback is their requirement to access the detector data from the scanner. These data are generally not readily available and proprietary in format, requiring specialist bespoke software from the scanner manufacturer, which is not openly available and requires assistance from the manufacturer for implementation [17, 22, 23]. Furthermore, some methods send noisy profile data back to a scanner for image reconstruction. This recourse to scanner manufacturers has hindered the research community [18].

This issue was addressed by Kim [3], Takenaga [23], and Naziroglu [24], who used image data as the data source and constructed projection data estimates to generate additive noise. Kim [3] and Naziroglu [24] presented comprehensive and complex methods and describe the challenges faced during implementation. For example, Kim [3] used a tapered multi-diameter circular phantom to derive the required parameters. Takenaga [23] considered a simpler approach, but only considered tube currents in the range of 300–100 mA (corresponding to 300–100 mAs) and did not account for electronic system noise, which becomes more significant at lower exposures.

The methods employed by the authors to validate the added noise generally focused only on the accuracy of the noise levels (variances), but not on the full noise characteristics, and did not assess how the textural nature varied over the entire field of view. Joemai [19], Yu [20], Kim [3], Takenaga [23], and Naziroglu [24] assessed noise characteristics by deriving the NPS, which is only central to the field of view and rotationally averaged. By reducing the NPS to one-dimensional (1D) spectra, it is not possible to assess the directionality of the frequency components and how they vary over the field of view, which is vital for evaluating noise characteristics. Naziroglu [24] and Elhamiasl [2] presented the two-dimensional (2D) spectra from noise-added images and compared them with those from scanner-acquired images.

In this study, we present a method for adding noise to CT images, which has the advantages of detector noise addition algorithms requiring only Digital Imaging and Communication in Medicine (DICOM) images as the data source, that is, without requiring proprietary detector profile data. DICOM images are generally provided as a standard item by contemporary CT scanning systems and, therefore, are readily available. The objectives of this study were to reproduce the complete, nonuniform, directional, and imaging subject-dependent noise characteristics using a simple computational implementation and requiring only widely available phantoms for calibration. This method was validated by assessing the standard deviations of noise over a range of regions and dose levels. The 2D noise spectra were derived

and assessed, and the mechanism by which the features in the spectra were generated was explained.

2 Methods

The remainder of this section is organized as follows. In the first subsection, we describe the equipment used and the image acquisition process. In the second subsection, we describe the method for adding noise to images. Finally, in the third subsection, we describe the experiment conducted to validate the noise addition process.

2.1 Equipment and image acquisition

An anthropomorphic thoracic phantom (QRM GmbH thoracic phantom, QRM, Mohrendorf, Germany) and a cylindrical acrylic phantom with a diameter of 320 mm were used in this study. Both phantoms were imaged using a 16-slice CT scanner (GE Lightspeed16, GE Healthcare, Waukesha, WIS, USA) following the protocol used in standard local clinical practice (120 kVp and 49 mAs) and at various reduced exposures (39, 34, 24, 17, and 5 mAs). The length of the thoracic phantom was 200 mm, which allowed the acquisition of 17 slices at 5-mm intervals over the central 80 mm to avoid any effects from being too close to the edge of the phantom. Although the acrylic phantom was longer, only 17 central slices were acquired at 5-mm intervals for consistency. A constant tube current was used with respect to both the gantry position (z-axis) and tube rotation during acquisition; that is, no automatic exposure control was used. The phantoms were positioned as close as possible to the isocenter and aligned axially to the scanner. All images (for both phantoms) were reconstructed using a soft-tissue setting appropriate for the chest phantom.

2.2 Method to add noise to images

Pixel data from a source image were forward projected to estimate radiation intensity projections. Poisson noise was added to the projection data to simulate the effect of lowering exposure, and the images were reconstructed by reversing the process using filtered back-projection. Processing and programming were performed in MATLAB (MathWorks Inc., Natick, MA, USA).

2.2.1 Extraction of attenuation data

For each source image, pixel data in Hounsfield units (HU) were obtained from the DICOM file and converted to linear attenuation coefficients $\mu(x,y)$ [25]. A value of 0.22 cm^{-1} was used for the linear attenuation of water, as this reflected the beam energy profile at 120 kVp. The attenuation

coefficients, representing the attenuation per unit length at each pixel position, were then converted to linear attenuation values across each pixel area by multiplying them by the pixel spacing obtained from the DICOM data. The values in the attenuation data matrix outside the (circular) field of view were set to zero.

2.2.2 Calculation of projection data

A Radon transform [26, 27] was applied to the attenuation data, which were summed along the rays to estimate the total attenuation along each projection path. For this purpose, a parallel-beam geometry was assumed and the projection angles were spaced at 0.5° intervals. These data were then converted into transmittance data $P(z,\theta)$ using the Beer–Lambert relationship [25].

2.2.3 Application of bowtie filter

A bowtie filter was incorporated into the imaging system. The exact parameters of the bowtie filter in the imaging system were unknown; therefore, a window function was chosen to approximate the typical bowtie filter used for imaging the abdomen and thorax, which was applied to all projections. The central 20 values (of the same sample spacing as the pixel spacing) of the window function used was considered as unity (100% transmittance). Outside this, the function decreased to a minimum value of 0.05 (5% transmittance) as a half sinusoid extended towards both edges of the field of view (at positions of 180 mm per 256-pixel spacing from the center), as shown in Fig. 2. The validation of this window function is presented in the Experimental Validation section. Notably, these bowtie filter parameters are only applicable to the field-of-view size under study and

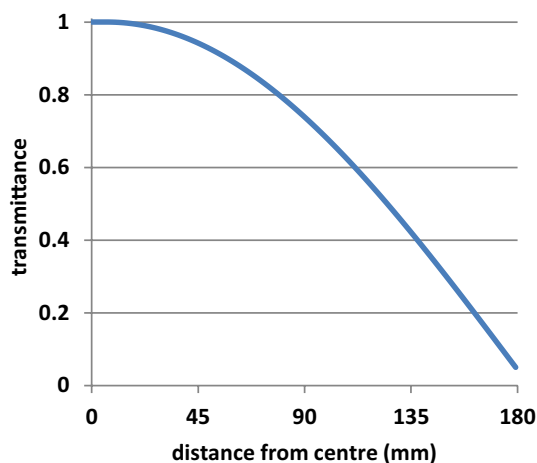


Fig. 2 Bowtie filter transmittance profile

would likely require modification if a different field-of-view size is chosen.

2.2.4 Addition of poisson noise to the projection data

The resulting estimate of the projection data is proportional to the X-ray energy incident on the detectors. Therefore, it is proportional to the number of quanta incident on the detectors (for a given beam energy profile). $P(z,\theta)$ was multiplied by the constant s determined by the calibration process described below, to estimate of the number of quanta Q incident on the detectors $Q(z,\theta) = sP(z,\theta)$. Stochastic noise was then added to the projection data by adding Poisson noise to $Q(z,\theta)$. As the variance of the Poisson noise is equal to its mean, parameter s governs the level of noise added across the image. Furthermore, the larger the value of $Q(z,\theta)$ at particular data points, the larger the variance of the noise added at those points, resulting in a variation in the noise magnitude required over the projections.

2.2.5 Reconstruction of images

Noise-added images were reconstructed by applying a reversal of the abovementioned process to the noisy projection data. The data were divided by parameters s , and each projection was windowed with the reciprocal of the bowtie filter. The logarithm of these data was used to apply the Beer–Lambert relationship, and an inverse Radon transform was applied with a reconstruction filter to derive the attenuation map, which was then converted back to HU. The inverse Radon Transform was implemented using the MATLAB (ray-driven) ‘iradon’ function.

A block diagram of this process is shown in Fig. 3.

2.3 Calibration of the noise addition method

The process required calibrating the parameters of the reconstruction filter applied in the last step of the process to back-project the data and parameter s , which governed the amount of noise added to affect the required target exposure and dose.

For the reconstruction filter, a ramp filter (where the filter coefficient is proportional to the frequency) was used, which was modified by weighting with an apodisation function to roll off at higher frequencies [24]. An apodisation function is generally chosen by the user to suit a particular scanning application such as bone or soft tissue. The apodisation function used in this study was selected based on an iterative experiment. A 32×32 -pixel region at the center of the cylindrical phantom was used for this part of the calibration process. An initial filter was chosen; coefficients 0–6 were unity, and those above this range had a half-cosine function that rolled off to zero at coefficient number 16. An initial

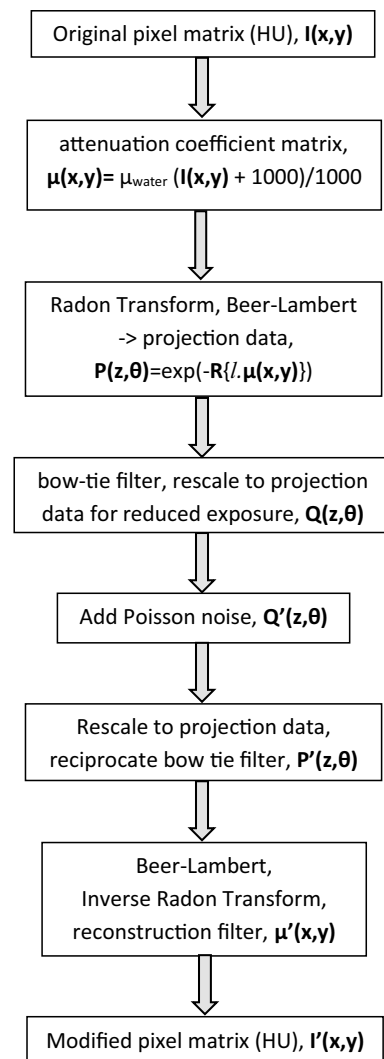


Fig. 3 Block diagram of the noise addition method

value for parameter s was determined by iteration, applying the noise addition process to a 49-mAs source image to produce the same noise standard deviation (averaged over the 17 available slices) as that in the center of the scanner-acquired images for a reduced mid-range exposure (34 mAs). The 2D fast Fourier transforms (FFTs) were derived for these central pixel regions in both the noise-added and scanner-acquired images. Each of these was rotationally averaged about its center (zero-frequency) point to obtain smoother 1D spectra (akin to the NPS [28]). These were averaged over the 17 available slices to obtain smoother spectra for both noise-added and scanner-acquired images. These 1D spectra were compared, and the filter parameters were adjusted iteratively until the spectra from the noise-added and scanner-acquired images were in the closest possible agreement. In addition, parameter s was adjusted to maintain the correct standard deviation of the pixel values. Only filter

coefficients numbered 7 and above were adjusted because we found that not doing so incurred reconstruction artifacts; the coefficients below this were maintained at unity. The central region of the cylindrical phantom was used. In this region, the 2D FFTs were expected to be rotationally symmetrical; therefore, rotationally averaging them was a valid approach.

The parameter s was dependent on both the source and target image exposures and on the highest exposure used in this process to account for electronic system noise. The value of this parameter was estimated experimentally to obtain the correct noise standard deviation in the target region of interest (ROI) of the final noisy image. The selected target regions were 32×32 -pixel regions close to the center of the mediastinal region of the thoracic phantom and just to the side of the central insert of the cylindrical phantom (Figs. 4c ROI3 and 4a ROI1). These regions were selected because they are the most uniform and near-central regions available. Both phantoms were used to encompass as large a detector dose range as possible, because the cylindrical phantom was significantly more attenuated than the thoracic phantom. Target standard deviations were determined by calculating the standard deviations in these regions for each

target exposure studied from the scanner-acquired images and calculating the means of these standard deviations over the 17 slices available for each.

The value of parameter s is dependent on several factors, and it is nontrivial to derive a theoretical formula; therefore, an expression for the best fit s across the range of exposures studied was derived experimentally and is expressed in Eq. 1.

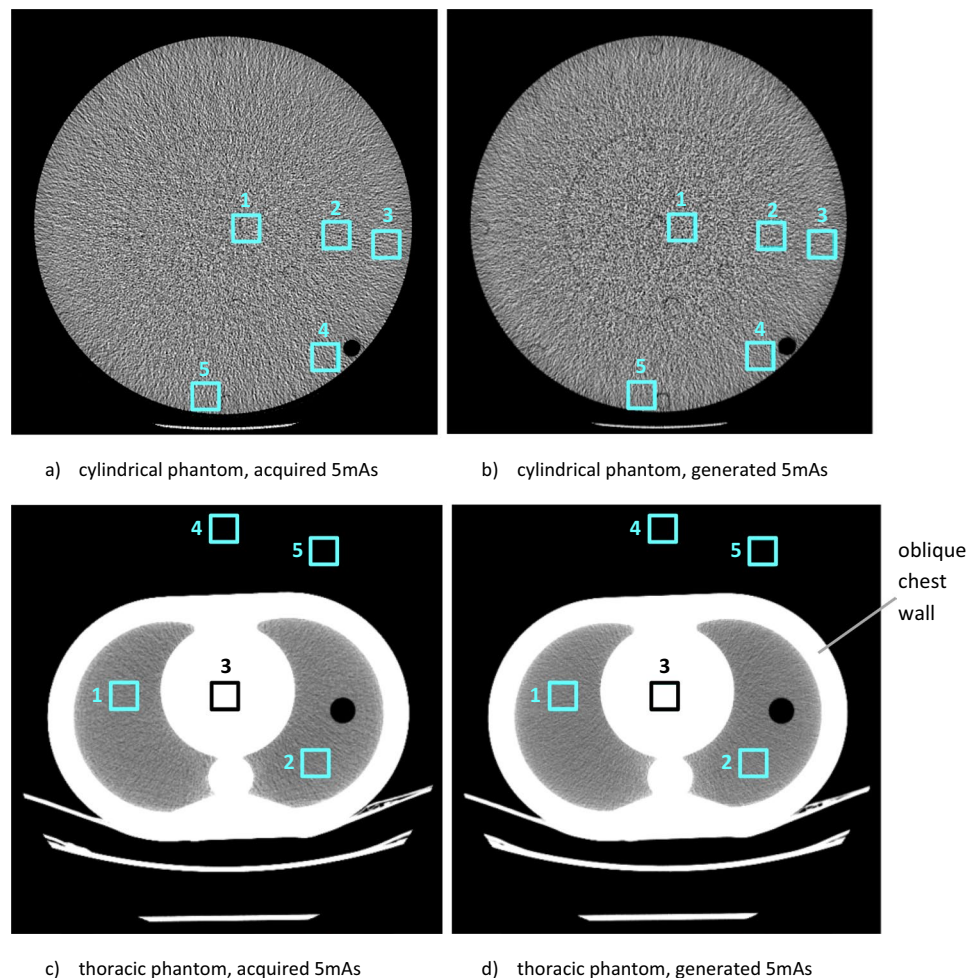
$$s(E_t, E_s, E_h) = (aE_t^2 + bE_t + c) \left(1 + d \left[\frac{1}{E_s} - \frac{1}{E_h} \right] E_t \right) \quad (1)$$

where E_t represents the target image exposure (tube current–time product, mAs), E_s represents the source image exposure (mAs), and E_h represents the highest exposure used (i.e., 49 mAs).

This is essentially a quadratic fit to the target image exposure (left bracket), modified by a factor to compensate for the noise initially present in the source image (right bracket).

Parameters a , b , c , and d were estimated as follows. The value of s was accurately determined for each pairwise combination of available exposures as the source and

Fig. 4 Examples of cylindrical and thoracic phantom images acquired at 5 mAs and those generated at 5 mAs from images originally acquired at 49 mAs, with regions of interest used in the analysis. The thoracic phantom images are windowed to demonstrate noise in the lung fields



target exposures. This was achieved by iteratively applying the proposed method and adjusting the s value to obtain the correct standard deviation of the target noise measured experimentally in the acquired reduced-exposure images. Subsequently, these values of s were plotted against target exposure E_t (for both phantoms) initially for only the highest source image exposure E_h (49 mAs) used in this study. A best-fit quadratic was fitted to s using the least squares method to yield parameters a , b , and c . To calculate the adjustment required for parameter s for other source exposures, a multiplicative factor was included (right bracket of Eq. 1). The parameters for this calculation were estimated by plotting the multiplicative factor against $[E_t/E_s - E_t/E_h]$. A best-fit straight-line fit was calculated, which passed through point (0,1), that is, no adjustment was required for $E_s = E_h$. The gradient of this line provided parameter d .

2.4 Experimental validation

To validate noise characteristics, images were generated for each combination of source and target exposures. These images were compared to those acquired from the scanner with the corresponding target exposure. Five regions of interest from the cylindrical and thoracic phantoms were selected for this comparison. These regions represent the range of noise characteristics present in the images, are locally stationary or as close to locally stationary as possible, and pose a challenge to the noise addition process. Furthermore, regions in the lung fields of the thoracic phantoms were chosen because of their clinical relevance; for example, in the investigation of lung nodules. All the regions were squares of 32×32 pixels, as shown in Fig. 4.

Seventeen images (axial slices) were available as source images for each exposure combination. Noise was added independently to each of these images using the proposed method for each target exposure and assessed as follows:

First, the noise magnitude in each region was quantified by measuring the standard deviation of the pixel values in each region. The mean standard deviations from each set of 17 images were calculated and compared with those from the corresponding regions of the images with the same target exposure acquired using the scanner.

Second, a more detailed investigation of the noise characteristics was conducted by calculating the 2D FFTs for each region of interest. Based on these FFTs, mean spectra were computed for each set of 17 images. These spectra were visually compared with those of the corresponding regions of the target exposure images acquired using the scanner. Full analysis or quantification of the characteristics was not performed on these spectra because this would have required more than 17 images to obtain sufficiently consistent spectra and yield meaningful results.

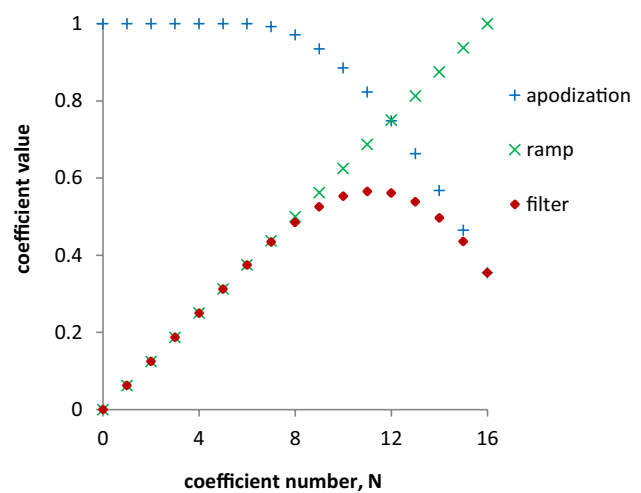


Fig. 5 Reconstruction filter coefficients

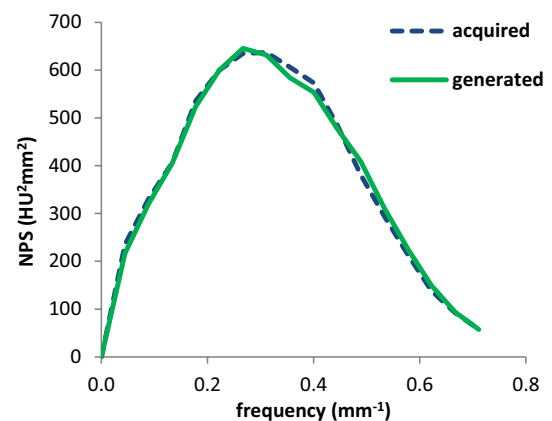


Fig. 6 One-dimensional noise spectra from the images of the center of the cylindrical phantom acquired at 34 mAs and from images generated at a target exposure of 34 mAs from those acquired at 49 mAs

3 Results

We found that the apodisation function that provided the best match to the noise from the acquired images was a half-cosine function that reached zero at the (would be) 19th filter coefficient (Fig. 5). To demonstrate the validity of this result, the 1D noise spectra for the central region of the cylindrical phantom from images acquired at 34 mAs and those from images generated by the noise addition process, including the reconstruction filter for 34-mAs target images from 49-mAs source images, were compared (Fig. 6).

The parameters a , b , c , and d required for the calculation of s were determined; these parameters are presented in Table 1.

Table 1 Parameters used in the calculation of parameter *s*

Parameter	Value
<i>a</i>	1.912×10^3
<i>b</i>	5.665×10^4
<i>c</i>	9.840×10^4
<i>d</i>	0.5845

An example of a noise-added image from both phantoms generated from a 49-mAs source image for a target exposure of 5 mAs, alongside the images acquired from the scanner at the same target exposure, is shown in Fig. 4. We found that the mean pixel values in the ROIs of the generated images and the corresponding ROIs of the phantom acquired images at any exposure were in very good agreement (see Online Resource 1).

The differences between the standard deviations of the generated noise and those of the noise in the scanner-acquired images for the corresponding exposures, expressed as percentages of the standard deviations of the target noise for each target exposure, are summarized in Table 2. These are the root mean square (RMS) values for the images generated from all source images used for each target exposure. *N* is the number of exposure combinations used for the target exposure, that is, the number of source exposures available for that target exposure. As 17 individual images were available for each combination of source-target exposures, the number of individual images used for each target exposure was $17 \times N$. A representative selection of these results is shown in Fig. 7. This selection was derived from 49-mAs source images, and includes ROI3 and ROI1 of the thoracic phantom that were the central region and one of the lung regions, respectively, and ROI1 and ROI4 of the cylindrical phantom that were the central region and one of the peripheral regions, respectively.

The standard deviations of the noise in the generated and acquired images were within one standard deviation for all source and target exposure combinations and for both phantoms, with only a small number of exceptions. These exceptions were for the lowest target exposure (5 mAs) across ROI2 to ROI5 of the cylindrical phantom and for the 17-mAs target exposure for ROI4. This is illustrated in Fig. 7, which shows that for ROI4 in the cylindrical phantom, the 5-mAs noise standard deviation was clearly not in agreement, but the 17-mAs target exposure was not quite in agreement. This was typical for all the source exposures at these target exposures, as indicated by the RMS differences presented in Table 2.

The RMS difference over all exposures and regions of interest in the thoracic phantom was 3.9% of the standard deviation of target noise (from 75 images), whereas that for the cylindrical phantom was 15%. In the cylindrical phantom, the RMS differences were noticeably greater for ROIs

Table 2 Standard deviations of pixel values in Hounsfield units for images acquired (target SD) over the range of exposures and root mean squares of differences between these and the corresponding standard deviations of pixel values from generated images for each ROI, where *N* is the number of available (and used) exposure combinations for generating images for each target exposure

Thoracic	Target mAs	<i>N</i>	ROI1			ROI2			ROI3			ROI4			ROI5			All ROIs		
			Target SD	RMS diff	RMS diff	Target SD	RMS diff	RMS diff	Target SD	RMS diff	RMS diff	Target SD	RMS diff	RMS diff	Target SD	RMS diff	RMS diff	Target SD	RMS diff	RMS diff
	39	1	2.9	2.4%	3.2	1.3%	4.4	1.1%	2.4	1.7%	2.4	1.1%	2.4	1.7%	2.4	3.8%	5	2.3%		
	34	2	3.0	1.1%	3.4	2.6%	4.8	0.9%	2.5	3.2%	2.5	0.9%	2.5	3.2%	2.5	6.1%	10	3.3%		
	24	3	3.7	4.7%	3.9	2.8%	5.7	0.9%	3	0.6%	3.0	0.9%	3	0.6%	3.0	3.9%	15	3.1%		
	17	4	4.3	3.0%	4.6	4.3%	6.8	1.1%	3.5	4.4%	3.5	1.1%	3.5	4.4%	3.5	6.0%	20	4.1%		
	5	5	7.2	3.0%	7.6	0.9%	12.4	0.8%	6.0	8.4%	6.0	0.8%	6.0	8.4%	6.0	4.3%	25	4.5%		
	Overall rms diff			3.2%		2.8%		1.0%		5.5%		1.0%		5.5%		5.0%		3.9%		
	Cylinder																			
	39	1	26	0.4%	20	4.0%	16	8.1%	18	0.6%	18	8.1%	18	0.6%	18	0.6%	5	4.1%		
	34	2	28	0.0%	22	1.6%	18	0.4%	20	4.5%	20	0.4%	20	4.5%	20	2.0%	10	2.3%		
	24	3	33	2.6%	27	1.0%	22	0.5%	25	8.8%	25	0.5%	25	8.8%	25	6.1%	15	5.0%		
	17	4	41	0.8%	35	7.1%	29	9.2%	32	14.0%	32	9.2%	32	14.0%	32	12.1%	20	9.8%		
	5	5	78	2.5%	77	22.1%	67	27.4%	69	28.1%	69	27.4%	69	28.1%	69	25.7%	25	23.2%		
	Overall rms diff			1.9%		13.3%		16.7%		18.3%		16.7%		18.3%		16.3%		15.0%		

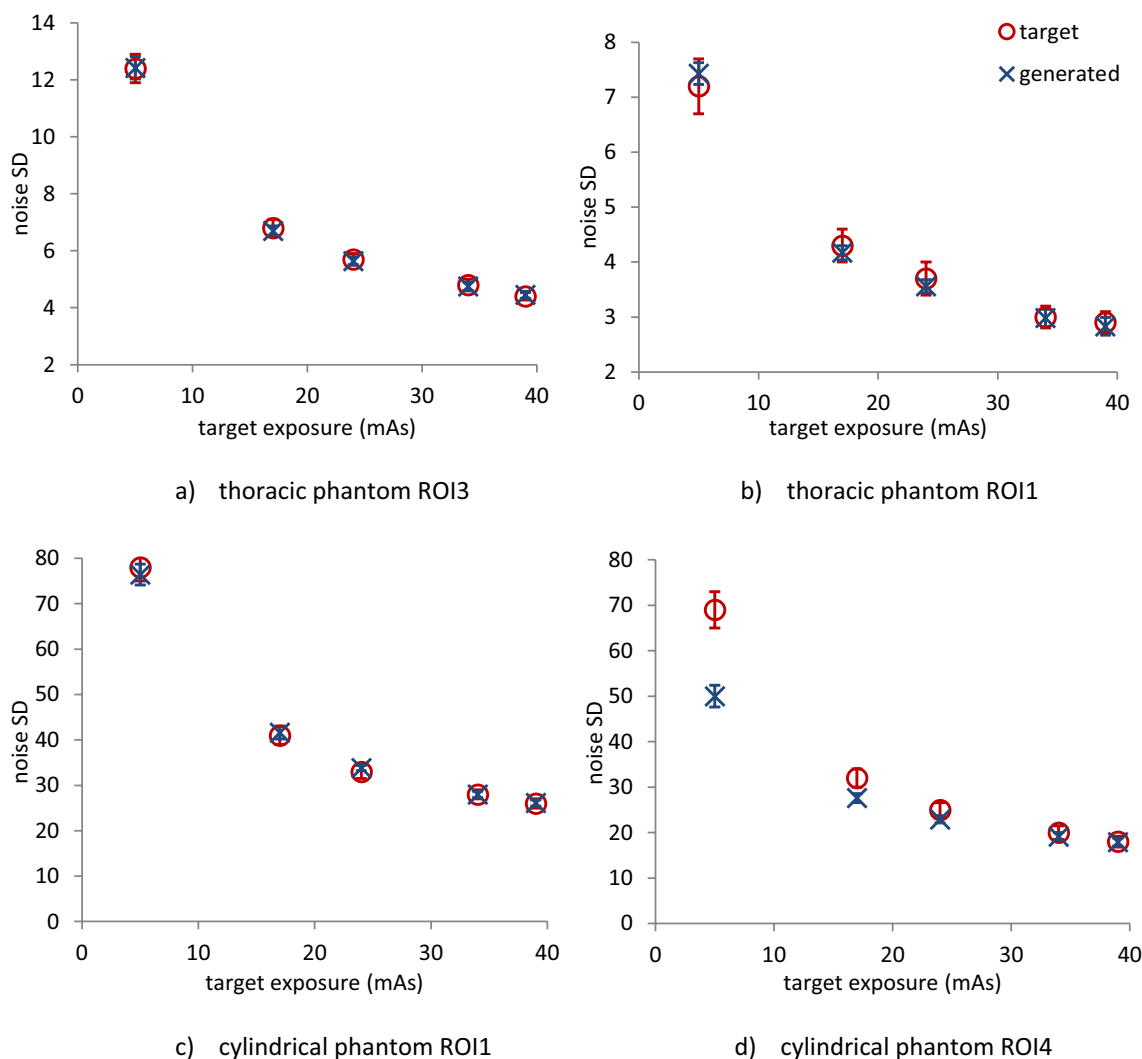


Fig. 7 Comparisons of noise standard deviations between images acquired at reduced exposures (O) and those generated at reduced exposures from images originally acquired at 49 mAs (X) for selected

ROIs. Error bars show one standard deviation (of noise standard deviations) of the 17 images available for each exposure

2–5 at the two lowest target exposures than for the remaining target exposures and for ROI1 at all target exposures. For the 17-mAs target exposure images and ROIs 3–5, the overall RMS difference was 11.9% (from 12 images), whereas for the 5-mAs target exposure images and ROIs 2–5, the overall RMS difference was 26%. The RMS difference of the remaining target exposures and ROIs was 4.1% (from 43 images), close to those of all target exposures and ROIs in the thoracic phantom (3.9%).

The 2D FFTs of each ROI in each phantom for the images acquired at the lowest exposure (5 mAs) and those generated at 5 mAs from the source images at 49 mAs are shown in Fig. 8. These spectra represent the mean spectra of the 17 available image slices. The lowest-exposure images are shown, as they provide the best visualization of the frequency components, as they have the largest magnitude. The

spectra of the images at other exposures exhibited similar characteristics for each corresponding ROI with lower-magnitude frequency components.

4 Discussion

The comparison of the 1D noise spectra derived from the central region of the images of the cylindrical phantom acquired at 34 mAs, with those generated from the 49-mAs images to a target of 34 mAs (Fig. 6), showed good agreement. This indicates that the noise characteristics are accurately reproduced by the proposed method in the central region and validates the choice of the reconstruction filter. For further comparison, 1-D noise spectra are shown for this region for a range of exposures in Online Resource 1, which

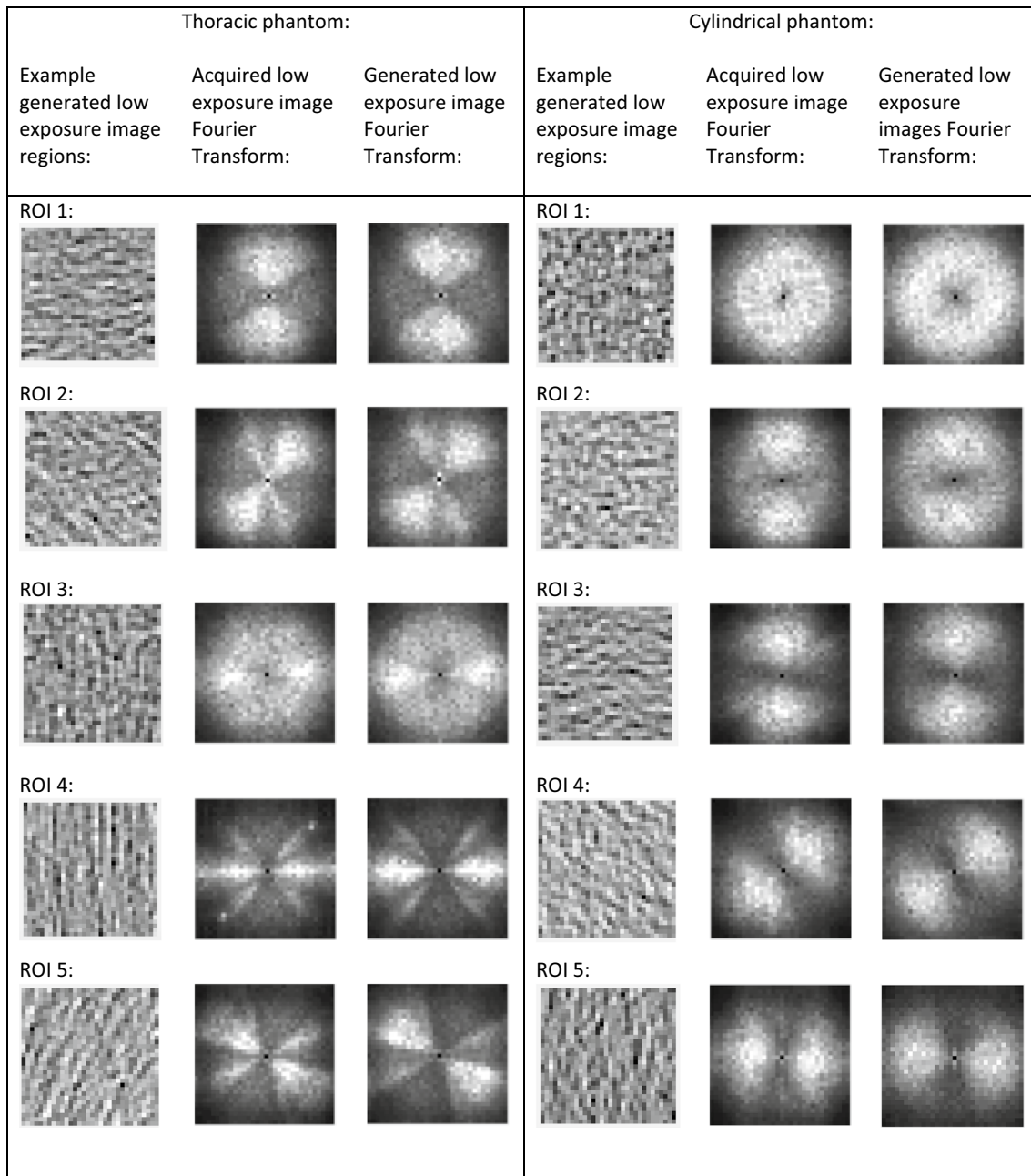


Fig. 8 Example image regions from images generated at a 5-mAs target exposure from 49-mAs source images with corresponding 2D Fourier transforms (mean of 17 available slices) and the corresponding Fourier transforms of images acquired at 5 mAs

generally show agreement between the acquired and generated data. Other areas of the cylindrical and chest phantom images would not be expected to produce rotationally symmetrical 2D FFTs; thus, rotationally averaging these 2D spectra to derive the 1D spectra would not be valid. This would require a 2D frequency-domain analysis approach, which was not possible in this study with only 17 slices available for averaging for each exposure, as the 2D spectra were too noisy. (Some examples of 1-D spectra sampled from the x- and y-frequency axes of the 2-D spectra are

shown in Online Resource 1 and demonstrate broad agreement between the acquired and generated data.)

For the images acquired from the thoracic phantom, noise amplitudes (standard deviations) showed good agreement between the acquired and generated images, with an RMS difference of 3.9% across all target and source image exposure combinations (Table 2). This difference was small when compared to the quantization noise generated from the expression of pixel values as integer HU values. The standard deviation of the quantization noise is $1/\sqrt{12}$ of a HU

[29], that is, 0.29 HU, compared with 3.9% of a mid-range noise's standard deviation of 4 HU, which is 0.16 HU. The agreement varies between regions of interest and exposures. Agreement for the cylindrical phantom was also comparably good, with an RMS difference of 4.1% over all regions and exposures except for the peripheral regions (ROIs3-5) at the lowest two exposures studied.

Agreement was particularly good for the central regions of interest for both phantoms over all exposures (RMS difference of 1% for the thoracic phantom ROI3 and 1.9% for the cylindrical ROI1). This was expected, because this region was used to calibrate the proposed method. Agreement was also good in the lung field regions of the thoracic phantom (ROI1 3.2% and ROI2 2.8%), which were the regions of most clinical relevance used in the study.

The peripheral regions in both phantoms showed less good agreement; in the case of the thoracic phantom, only slightly so (5.5% and 5.0% for ROI4 and ROI5, respectively), these regions are unlikely to be clinically relevant because they are outside the phantom and outside the habitus of a typical patient. Differences were more significant in peripheral regions of the cylindrical phantom (between 16.3% and 18.3% for ROIs3-5). In these regions, in both phantoms and close to the edges of the field of view, the modelling of the system may be less accurate than in the central regions because of the use of a parallel-beam model in the proposed method, which does not reflect the true CT system geometry. In the cylindrical phantom, these differences may have been exacerbated by beam hardening in the acrylic from which it was composed, which is considerably more attenuating than in the thoracic phantom, resulting in a higher effective keV of X-rays. Consequently, a lower linear attenuation of the water coefficient is required in Eq. (1) to model the cylindrical phantom more accurately. Although the accuracy of the method was low at very low target exposures in the periphery of the cylindrical phantom, lower exposures of down to 5 mAs were used in this study compared with those used in studies by other authors.

All 2D frequency spectra plots showed remarkable agreement between the acquired low-exposure images and the generated images for the corresponding regions of interest in both phantoms (Fig. 8). The peaks present in the spectra from the scanner-acquired images correspond very closely to the peaks in the corresponding noise-added images.

In the cylindrical phantom, the spectra of the central region (ROI1) were in the form of a broad disk (torus) centered on the origin with no sharp peaks. This is because the attenuation around this region is equally distributed at all angles, giving rise to noise with no particular directional component and noise spectra with infinite rotational symmetry.

The spectra from all other regions also showed the same torus in the background with various superposed peaks.

These peak components in the frequency space were always normal to the spatial directionality of the noise in the corresponding image and were always in pairs opposite each other with respect to the origin (as per the Fourier Transform theory [29]). The noise is always oriented along the direction of the attenuation peak from the image region, as per Kalender [15].

For example, in the cylindrical phantom, the area of greatest attenuation from ROI3 was towards the phantom center, that is, to its left-hand side, producing noise in the image oriented in the x-axis direction and a pair of frequency components positioned along the y-frequency axis in its 2D FFT. In ROI4 to ROI5, the directionality of the noise and frequency components moved approximately from 45° to 90°, respectively, as the position of the center of the phantom moved similarly with respect to these regions. The peaks in ROI2 were in the same position as those in ROI3, but were less prominent as ROI2 was closer to the center of the phantom; therefore, the differences in attenuation around ROI2 were smaller.

In the thoracic phantom, spectral components were observed at various positions corresponding to several areas of local attenuation maxima. ROI1 showed components generated from the mediastinum and ROI3 showed components obtained from the vertebra. ROI2 showed peaks generated from both anatomical regions at different positions to those for ROI1 and ROI3 because these locally higher attenuating areas were positioned at different angles relative to ROI2. Similarly, ROI4 and ROI5 showed components generated from both the mediastinum and vertebra, as well as from the ribs/chest wall at various angles. This finding is additional to that of Kalender [15], who noted that noise patterns in computed tomography are oriented in the direction of the highest attenuation. We observed that multiple local peaks in attenuation around an ROI gave rise to multiple peaks in the spectra and multiple corresponding noise directionalities.

ROI4 in the thoracic phantom was the only region in which a significant difference between the acquired and generated low-dose spectra was observed. There was a sharp frequency component pair 45° above the x-frequency axis and at a high frequency (i.e., towards the periphery of the 2D FFT) in the acquired image, which was not observed in the generated image. This was attributed to the presence of artifacts that appeared as patches around this region on some slices of the acquired images, consisting of a regular series of lines running 45° below the x-axis. This may be because of undersampling in the image acquisition process [30] and not because of the noise addition process.

Although we demonstrated that the generated noise was similar to real noise, there were some sources of error in the process. These included errors in the measurement of the noise amplitude from the scanner-acquired images from which the amplitudes of the source and target noises were

obtained, and consequently, errors in the parameters calibrating the process. Only 17 slices were available from both the phantoms for each exposure. This error can be reduced by repeated scanning to obtain more images, from which the average noise standard deviations can be obtained, resulting in more accurate calibration parameters and smoother spatial-frequency plots. The findings of this study demonstrate the potential of the proposed method.

The model uses a parallel beam projection as an approximation of the diverging beam in a practical scanner geometry. This is likely to have accounted for the minor differences in the prominence of some peaks in the frequency plots, although the observed positions of these peaks were accurate. Similarly, the image construction process was modeled only on a slice-by-slice basis, and a multiple-row detector with a helical scanning process was not considered. Incorporating this into the model may be possible; however, it is a complex process that may improve generalizability. The model proposed in this study was adequate for the phantoms used to calibrate and evaluate the noise addition process given that their geometry did not vary in the gantry axis direction.

This method is based on an estimate of the detector data and inevitably includes errors generated from the forward-projected image noise in the initial step. Because the image noise is small (with a standard deviation of up to 12 HU in the thoracic phantom) compared to the signal (within a range of a few thousand HU), this should not be significant.

This method uses the assumed characteristic of the bowtie filter. The method may be improved by either obtaining the actual specifications of the filter, which was not possible, or by experimentally using an in-air scan, as suggested by Masoumzadeh (2009) and Yu (2012), which would be relatively straightforward. Although these authors used detector data as the data source in their method, the detector data could be adequately estimated from the image using the initial steps of the method described above.

Automatic exposure controls were not used in this study. These controls can be incorporated into the proposed method by estimating the exposure modulation from the estimated profile data, as implemented by Yu (2012); however, Yu used detector data directly. The incorporation of automatic exposure control into the proposed method is relatively straightforward.

Calibration was applied to this setup, as previously described. The calibration process should be repeated if the field-of-view size, bowtie filter or reconstruction filter, kVp, or beam filtering are changed or if exposure outside the range of 5–49 mAs is required. Without further validation, this method should not be applied when automatic exposure control is used.

One limitation of the proposed method is that it is applicable only to linear reconstructions. Nonlinear and iterative

reconstruction methods were outside the scope of this study because such iterative algorithms were not available to the experimenters. In principle, the proposed method, that is, the addition of stochastic noise to profile data estimated from DICOM image data, may also be applied to images both derived and reconstructed using other reconstruction methods; however, this requires further investigation.

In contemporary CT literature, there is focus on using machine learning, particularly deep learning and neural networks, to reduce image noise for image enhancement [31–33]. This may also be a suitable approach for adding noise to CT images. However, one drawback of this approach is that an extremely large number of images are required.

This method used a simple cylindrical acrylic phantom and a readily available thoracic phantom for calibration. Because only uniform and central regions of the phantoms were required for this calibration, a simple cylindrical water phantom would be sufficient if a thoracic phantom was not available.

In summary, a practical method for adding noise to CT images that requires only easily accessible DICOM images as source data and simple, readily available phantoms for calibration is presented. Therefore, it is suitable for use in future observational and dose-reduction studies. Cylindrical acrylic and thoracic phantoms are used to validate the generated noise characteristics. The standard deviations of the generated noise and the 2D local spatial frequency characteristics were found to be a good match to the corresponding scanner-acquired lower-exposure images over a range of exposures from 39 mAs to below 20 mAs.

Supplementary Information The online version contains supplementary material available at <https://doi.org/10.1007/s12194-023-00755-w>.

Acknowledgements The authors gratefully thank Andy Rogers for assistance with scanning and the CT department at Nottingham City Hospital for access to their CT scanners.

Declarations

Conflicts of interest The authors did not receive support or funding from any organization for the submitted work. The authors have no relevant financial, non-financial or competing interests to disclose.

Ethics approval This study did not involve any human participants, therefore, no ethical approval was required.

Informed consent This study did not involve any human participants therefore no informed consent was required.

References

1. Brenner DJ, Hall EJ. Computed tomography- An increasing source of radiation exposure. *N Engl J Med.* 2007;357:2277–84.

2. Elhamiasl M, Nuyts J. Low-dose x-ray CT simulation from an available higher-dose scan. *Phys Med Biol.* 2020;65: 135010.
3. Kim CW, Kim JH. Realistic simulation of reduced-dose CT with noise modelling and sonogram synthesis using DICOM CT images. *Med Phys.* 2014;41:011901–11.
4. Kalendar WA, Wolf H, Suess C, et al. Dose reduction in CT by on-line tube current control: principles and validation on phantoms and cadavers. *Eur Radiol.* 1999;9:323–8.
5. Singh S, Kalra MK, Moore MA, et al. Dose reduction and compliance with pediatric CT protocols adapted to patient size, clinical indication and number of prior studies. *Radiology.* 2009;252:200–8.
6. Karmazyn B, Frush DP, Applegate KE, et al. CT with a computer-simulated dose reduction technique for detection of pediatric nephroureterolithiasis: comparison of standard and reduced radiation doses. *Am J Roentgenol.* 2009;192:143–9.
7. Guimaraes LS, Fletcher JG, Harmsen WS, et al. Appropriate patient selection at abdominal dual-energy CT using 80 kV: relationship between patient size, image noise and image quality. *Radiology.* 2010;257:732–42.
8. Riederer SJ, Pelc NJ, Chesler DA. The noise power spectrum in computed X-ray tomography. *Phys Med Biol.* 1978;23:446–54.
9. Hanson KM. Detectability in computed tomographic images. *Med Phys.* 1979;6:441–51.
10. Kijewski MF, Judy PF. The noise power spectrum of CT images. *Phys Med Biol.* 1987;32:565–75.
11. Hsieh J. Nonstationary noise characteristics of the helical scan and its impact on image quality and artifacts. *Med Phys.* 1997;24:1375–84.
12. Wunderlich A, Noo F. Image covariance and lesion detectability in direct fan-beam X-ray computed tomography. *Phys Med Biol.* 2008;53:2471–93.
13. Baek J, Pelc NJ. The noise power spectrum in CT with direct fan beam reconstruction. *Med Phys.* 2010;37:2074–81.
14. Frush DP, Slack CC, Hollingsworth CL, et al. Computer-simulated radiation dose reduction for abdominal multidetector CT of pediatric patients. *Am J Roentgenol.* 2002;179:1107–13.
15. Kalendar WA, Buchenau S, Deak P, et al. Technical approaches to the optimisation of CT. *Physica Med.* 2008;24:71–9.
16. Hanson KM. Spectral analysis of non-stationary CT noise, International Symposium and Course on Computed Tomography, Los Alamos Scientific Laboratory, Las Vegas, [Los Alamos National Laboratory Web Site]. April 9, 1980. Available at <https://kmlanl.hansonhub.com/talks/ct80.abs.html>. Accessed August 31, 2021.17.
17. Britten AJ, Crotty M, Kiremidjian A, et al. The addition of computer simulated noise to investigate radiation dose and image quality in images with spatial correlation of statistical noise: an example application to X-ray CT of the brain. *Br J Radiol.* 2004;77:323–238.
18. Massoumzadeh P, Don S, Hildebolt CF, et al. Validation of CT dose-reduction simulation. *Med Phys.* 2009;36:174–89.
19. Joemai RM, Geleijns J, Veldkamp WJ. Development and validation of a low dose simulator for computed tomography. *Eur Radiol.* 2010;20:958–66.
20. Yu L, Shiung M, Jondal D, et al. Development and validation of a practical lower-dose-simulation tool for optimizing computed tomography scan protocols. *J Comput Assist Tomogr.* 2012;36:477–87.
21. Zabic S, Wang Q, Morton T, et al. A low-dose simulation tool for CT systems with energy integrating detectors. *Med Phys.* 2013;40: 031102.
22. Zeng D, Huang J, Bian Z, et al. A simple low-dose x-ray CT simulation from high-dose scan. *IEEE Trans Nucl Sci.* 2015;65:2226–33.
23. Takenaga T, Katsuragawa S, Goto M, et al. A computer simulation method for low-dose CT images by use of real high-dose images: a phantom study. *Radiol Phys Technol.* 2016;9:44–52.
24. Naziroglu RE, van Ravesteijn VF, van Vliet LJ, et al. Simulation of scanner-and patient-specific low-dose CT imaging from existing CT images. *Phys Medica.* 2017;36:12–23.
25. Hsieh J. *Computed tomography principles, design, artefacts and recent advances.* Bellingham, Washington, USA: SPIE Press; 2003.
26. Bracewell RN, *Imaging T-D.* Englewood Cliffs, NJ: Prentice Hall; 1995. p. 505–37.
27. Lim JS, *Signal T-D, Processing I.* Englewood Cliffs, NJ: Prentice Hall; 1990. p. 42–5.
28. Boone JM, Brink JA, et al. Radiation dose and image-quality assessment in computed tomography, *ICRU.* 2012;12:121–34.
29. Lathi BP. *Modern Digital and Analog Communication Systems.* New York: Holt Saunders; 1983.
30. Platten D, *Understanding Imaging Performance (3); Artefacts, ImPACT course,* [ImPACT CT scanner evaluation group Web Site]. Oct 2005. Available at <http://www.impactscan.org/slides/impactcourse/artefacts/index.html>. Accessed August 31, 2021.
31. Yang W, Zhang JY, Wu J, et al. Improving low-dose CT image using residual convolutional network. *IEEE Spec Sect Adv Sign Process Methods Med Imag.* 2017;5:24698–705.
32. Han Y, Framing YJC. U-Net via deep convolutional framellets: Application to sparse-view CT. *IEEE Trans Med Imag.* 2018;37:1418–29.
33. Liu B, Liu J. Overview of Image Denoising Based on Deep Learning. *J Phys Conf Ser.* 2019;1176:22010.

Publisher's Note Springer Nature remains neutral with regard to jurisdictional claims in published maps and institutional affiliations.